EDGE ARTICLE

Check for updates

Near-infrared AIEgens with high singlet-oxygen yields for mitochondria-specific imaging and antitumor photodynamic therapy†

Shasha Zhang,[a] Wenfang Yang,[a] Xiao Lu,[b] Xinyi Zhang,[a] Zhichao Pan,[a] Da-Hui Qu, [ID][a] Dong Mei,*[b] Ju Mei [ID] *[a] and He Tian [ID] [a]

AIE-active photosensitizers (PSs) are promising for antitumor therapy due to their advantages of aggregation-promoted photosensitizing properties and outstanding imaging ability. High singlet-oxygen ($^1O_2$) yield, near-infrared (NIR) emission, and organelle specificity are vital parameters to PSs for biomedical applications. Herein, three AIE-active PSs with D−π−A structures are rationally designed to realize efficient $^1O_2$ generation, by reducing the electron−hole distribution overlap, enlarging the difference on the electron-cloud distribution at the HOMO and LUMO, and decreasing the ΔE_{ST}. The design principle has been expounded with the aid of time-dependent density functional theory (TD-DFT) calculations and the analysis of electron−hole distributions. The $^1O_2$ quantum yields of AIE-PSs developed here can be up to 6.8 times that of the commercial photosensitizer Rose Bengal under white-light irradiation, thus among the ones with the highest $^1O_2$ quantum yields reported so far. Moreover, the NIR AIE-PSs show mitochondria-targeting capability, low dark cytotoxicity but superb photo-cytotoxicity, and satisfactory biocompatibility. The *in vivo* experimental results demonstrate good antitumor efficacy for the mouse tumour model. Therefore, the present work will shed light on the development of more high-performance AIE-PSs with high PDT efficiency.

Introduction

Photodynamic therapy (PDT), due to its site-specificity and non-invasiveness, has become one of the most promising strategies for clinical tumour treatment.[1–13] Exploiting photosensitizers (PSs) effectively generating reactive oxygen species (ROS) such as singlet oxygen ($^1O_2$) under light irradiation is of paramount importance to the development of PDT.[1,3–6,8] Among the PSs developed,[1–17] the luminescent ones usable for image-guided PDT are attracting increasing attention.[1–5,8,9,11,15–17] For a clinically usable luminescent PS, high ROS generation, long emission wavelength, and organelle specificity are very important factors.[2,4] However, most of the existing luminescent PSs still can hardly simultaneously hold these three merits.

[a] Key Laboratory for Advanced Materials, Joint International Research Laboratory of Precision Chemistry and Molecular Engineering, Feringa Nobel Prize Scientist Joint Research Center, Frontiers Science Center for Materiobiology and Dynamic Chemistry, Institute of Fine Chemicals, School of Chemistry & Molecular Engineering, East China University of Science & Technology, 130 Meilong Road, Shanghai 200237, P. R. China. E-mail: daisymeiju@ecust.edu.cn

[b] Clinical Research Center, Beijing Children's Hospital, Capital Medical University, National Center for Children's Health, 56 South Lishi Road, Xicheng District, Beijing 100045, P. R. China. E-mail: meidong@bch.com.cn
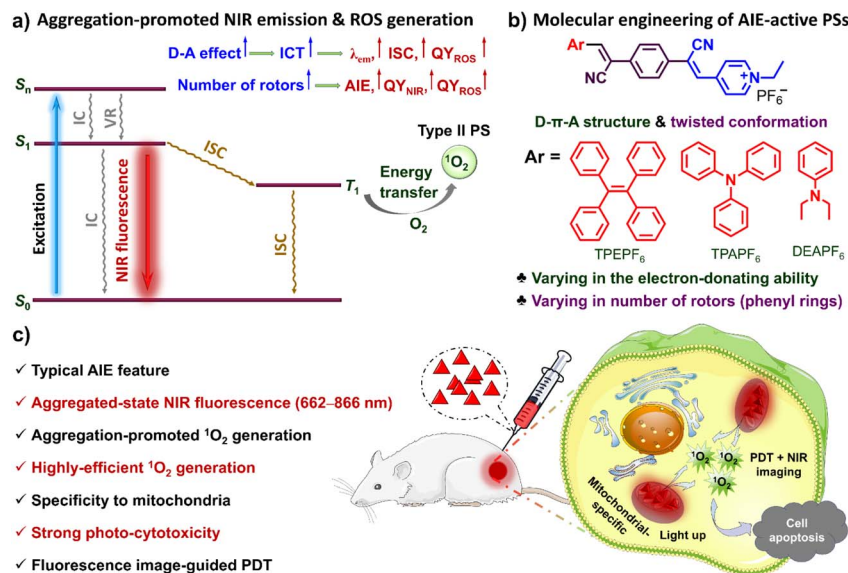
Small-molecular organic fluorophores with photosensitizing properties stand out among various PSs, due to their satisfactory biocompatibility and biodegradability, easy-to-adjust structures, and optical properties.[1–5,8,9,11–13,15–17] However, traditional organic luminescent PSs usually suffer from the aggregation-caused quenching (ACQ) effect in the biological media due to the rigid planar π-conjugated structures and poor water-solubility.[13,16,17] The ACQ effect of a luminescent PS usually leads to a reduction in the efficiency of emission and $^1O_2$ generation and subsequently limits its wide application in biomedical fields. In contrast, aggregation-induced emission (AIE)-active luminogens (AIEgens) have shown significant advantages and potential for biomedical applications due to their high brightness, outstanding photostability, and long-term *in situ* imaging ability.[5,8–11,14,15,18–37] What is more attractive is that the strong intra/intermolecular interactions make the AIEgens prone to form tighter aggregates, which could block the non-radiative pathways, increase the quantum yield, stabilize the triplet state, and thus boost the generation of ROS.[5,8,37] It is therefore believed that the AIEgen-based PSs are ideal candidates for image-guided PDT.[5,9,11,23,25,27,29,37]

NIR fluorescence imaging has shown great potential in the diagnosis of diseases such as cancer, due to its negligible bio-substrate autofluorescence interference and deep-tissue penetrating ability.[9,11,24,33,36] As such, developing simple and facilely accessible AIE-active NIR PSs is thus urgently needed to promote clinical applications. Moreover, organelle specificity is also conducive to the performance of luminescent PSs. Mitochondria-

Scheme 1 (a) Molecular design for high-performance NIR-emissive AIE-active PSs for image-guided efficient PDT. (b) Molecular engineering of NIR AIE-PSs, *i.e.*, TPEPF$_6$, TPAPF$_6$ and DEAPF$_6$. (c) Schematic illustration of the corresponding properties of the designed NIR AIE-PSs and the mitochondria-specific image-guided PDT effect of TPAPF$_6$. AIE: aggregation-induced emission; NIR: near-infrared; D–A effect: electron-donating and electron-accepting effect; ICT: intramolecular charge transfer; PDT: photodynamic therapy; PSs: photosensitizers; ISC: inter-system crossing; ROS: reactive oxygen species; $^1O_2$: singlet oxygen; QY$_{NIR}$: quantum yield of NIR fluorescence; QY$_{ROS}$: quantum yield of ROS.

specific PSs provide a favourable option for high-efficiency PDT,[33,34,36] because mitochondria are the energy factories for cells and key regulators of cell death signals.[38] On the other hand, mitochondria are the primary targeted sites of $^1O_2$, which are damaged in the early stages of apoptosis induced by PDT. Despite that AIE-active NIR PSs have been developed for mitochondria-specific image-guided PDT,[34,36,39–41] currently there is still a lack of simple and economical ones with high ROS yield and mitochondria-targeting ability.

Herein, three NIR AIE-active PSs (*i.e.*, TPEPF$_6$, TPAPF$_6$ and DEAPF$_6$) with mitochondria specificity and ultra-efficient $^1O_2$ generation have been developed through rational molecular engineering (Scheme 1a and b). Impressively, TPEPF$_6$ and TPAPF$_6$ show the highest $^1O_2$ quantum yields reported so far (Table S1†). The *in vitro* experiments have shown that the present AIE-PSs can be quickly taken up by cancer cells and display bright NIR fluorescence in cells, exhibiting high photostability, good biocompatibility, and preferable localization in mitochondria. In order to simply evaluate the PDT potential of these small-molecular AIE-PSs, we adopted the intratumoral injection to ensure their accumulation in tumours. The *in vivo* experiments have demonstrated the potential of these PSs to visualize tumours, efficiently destroy cancer cells and prevent the growth of malignant tumours under white-light irradiation (Scheme 1c). This research work is supposed to not only provide powerful alternatives for NIR fluorescence image-guided PDT but also offer insights into the rational design of efficient NIR-luminescent AIE-PSs.

Results and discussion

Molecular design, synthesis, and characterization

As shown in Scheme 1, in each of our AIE-PSs, twisted conformation, extended π-conjugation, donor–acceptor (D–A)

electronic structures, as well as the sufficient separation of the highest occupied molecular orbital (HOMO) and the lowest unoccupied molecular orbital (LUMO) have been ingeniously integrated. Structurally speaking, the twisted conformation with multiple rotors is believed to be responsible for the AIE attribute. To be more specific, the multiple aromatic rings connected through single bonds can rotate or twist around the single bonds and thus can be viewed as rotors. In the solution or molecularly dispersed state, the multiple aromatic rings can rotate freely and vigorously, which dissipates the excited-state energy, boosts the nonradiative decay channels, and thus leads to inefficient or even no emission. In contrast, in the solid or aggregated state, the intense intermolecular interactions exert physical constraints on the intramolecular motions, which activates the radiative decay pathways and results in efficient luminescence. Moreover, because of the repulsive interaction and the steric hindrance, the aromatic rings are tilted out of the plane, leading to a distorted 3D conformation. Such a conformation could prevent the π–π stacking and further hamper the emission quenching. Consequently, the AIE characteristics can be ensured. The extended π-conjugation together with the D–A structure is supposed to account for the NIR fluorescence and ICT effect. In the meantime, the ICT and the small overlap between the HOMO and LUMO, which for one thing reduce the energy gap between the singlet state and the triplet state (ΔE_{ST}) and for another promote the intersystem crossing (ISC), are supposed to contribute to the efficient PS effect.[5,8,37,42–46] What's more, it has been discovered that the separation of electron–hole transition orbitals is associated with the ICT effect, can give rise to a small ΔE_{ST} and accelerate the ISC process, thus conducive to the generation of ROS.[5,8,37,47–50]

Accordingly, molecules holding a D–π–A structure with multiple rotors are facilely constructed. Electron-donating

tetraphenylethylene (TPE), triphenylamine (TPA), and diethylaminobenzene (DEA) are respectively conjugated to the same electron-accepting moiety, *i.e.* (*E*)-4-(2-cyanovinyl)-1-ethylpyridin-1-ium groups *via* two simple Knoevenagel condensation reactions by using the intermediate of 2,2′-(1,4-phenylene)diacetonitrile. It thus gives rise to the uncharged molecular skeleton supposed to have an AIE feature and long-wavelength emission. Further salification of the pyridinyl groups successfully yields our targeted molecules TPEPF$_6$, TPAPF$_6$, and DEAPF$_6$ (Scheme 1). The positively charged pyridinium group not only can serve as an electron-accepting unit but also might afford a good mitochondria-targeting function.[33,34,40,41] The simple three-step synthetic routes of the designed TPEPF$_6$, TPAPF$_6$, and DEAPF$_6$ are shown in Scheme S1.† The structures of all the intermediates and targeted products were confirmed by ^{1}H NMR, ^{13}C NMR, and HRMS, with the detailed characterization data shown in Fig. S1–S25.†

Theoretical calculations

To grasp an understanding on the relationship between the structure and the properties of these three compounds prior to the experiments, the TD-DFT method in the Gaussian 09 software package was first applied to perform the structure optimization and theoretical calculations.[51] As revealed by the optimized molecular geometries shown in Fig. 1a, all these compounds adopt a non-planar conformation. It would

effectively inhibit the intermolecular π–π stacking and the subsequent fluorescence quenching and hence would allow these compounds to fluoresce intensively in the aggregated state. The energy gaps (E_gs) of TPEPF$_6$, TPAPF$_6$, and DEAPF$_6$ were calculated to be 2.06, 1.96, and 2.10 eV, respectively. Moreover, each compound exhibits distinctly different electron distributions between the HOMO and LUMO (Fig. 1a), suggestive of a remarkable ICT effect. The electron clouds on all the LUMOs are mainly distributed over the (*Z*)-4-(2-cyano-2-phenylvinyl)pyridin-1-ium moiety. Compared with TPEPF$_6$ and TPAPF$_6$, the electron cloud of the HOMO in DEAPF$_6$ is more widely distributed on the benzene in the middle of the 2,2′-(1,4-phenylene)diacrylonitrile group. It means that the charge separation is more thorough in TPEPF$_6$ and TPAPF$_6$ as compared to that in DEAPF$_6$. It implies that these compounds might all possess efficient PS properties, and the PS performances of TPEPF$_6$ and TPAPF$_6$ would probably be better than that of DEAPF$_6$. Taking the efficient ICT effect and small E_g together, NIR fluorescence can be anticipated as well.

To gain a deeper insight into their ICT effects, the electron–hole distributions were further analysed using the Multiwfn program.[47,48,52] The results are well consistent with those obtained *via* Gaussian calculations. More specifically, the calculated electron–hole distributions of these molecules in the S$_1$ state show that the electrons are mainly distributed on the (*Z*)-4-(2-cyano-2-phenylvinyl)pyridin-1-ium group (A), while the holes

Fig. 1 (a) Optimized geometries and molecular orbitals of the HOMO and LUMO levels of TPEPF$_6$, TPAPF$_6$, and DEAPF$_6$. (b) (Top panel) Electron–hole distributions of the S$_1$ states of TPEPF$_6$, TPAPF$_6$, and DEAPF$_6$. The blue regions depict where the electron densities are depleted, and the green regions depict where the electron densities are accumulated; (Bottom panel) Overlap of the electrons and holes for the S$_1$ state of the TPEPF$_6$, TPAPF$_6$, and DEAPF$_6$, respectively. (c) Singlet (S$_1$)- and triplet (T$_1$)-state energy levels of TPEPF$_6$, TPAPF$_6$, and DEAPF$_6$, respectively.

Table 1 The photophysical, electrochemical, and photosensitizing properties and the energy levels

Comp.	Soln./nm		Aggr./nm	Solid/nm	$HOMO^e$/eV	$LUMO^f$/eV	E_g^g/eV	$HOMO^h$/eV	$LUMO^h$/eV	E_g^h/eV	S_1^h/eV	T_1^h/eV	ΔE_{ST}^h/eV	E_{SOG}^i/nmol	Relative $^1O_2$ yield^j
	λ_{abs}^a	λ_{em}^b	λ_{em}^c	λ_{em}^d											
TPEPF$_6$	419	553	662	694	−5.77	−3.99	1.78	−5.67	−3.61	2.06	2.05	1.59	0.46	37.7	5.11
TPAPF$_6$ (crystal)	476	583	783	833	−5.48	−3.97	1.51	−5.49 (−5.48)	−3.53 (−3.86)	1.96 (1.62)	1.94 (1.65)	1.48 (1.34)	0.46 (0.31)	40.2	3.17
DEAPF$_6$	495	640	768	866	−5.59	−3.40	2.19	−5.56	−3.46	2.10	2.06	1.50	0.56	19.8	0.88

^{a} Absorption maximum in DMSO. ^{b} Emission maximum in DMSO. ^{c} Emission maximum in the DMSO/toluene mixture (1/9, v/v). ^{d} Emission maximum in the solid state. ^{e} Obtained from the onset of the oxidation voltages using the equation: $E_{HOMO} = -e(E_{onset\ ox} + 4.4\ V)$. ^{f} Obtained from the onset of the reduction voltages using the equation: $E_{LUMO} = -e(E_{onset\ re} + 4.4\ V)$. ^{g} Obtained from the equation: $E_g = E_{LUMO} - E_{HOMO}$. ^{h} Values obtained from DFT calculation using the Gaussian 09 package. ^{i} O$_2$ generation, which was calculated by monitoring the amount of ABDA consumed per minute in the presence of 10 nmol of AIE-PS under white-light irradiation (25 mW cm^{-2}). [ABDA] = 5 × [AIE-PS]. ^{j} The relative ^{1}O$_2$ generation efficiencies were measured under the same conditions as Rose Bengal (RB = 0.75 in water) which was employed as the standard.

are primarily distributed on the acrylonitrile-decorated TPE/TPA/DEA group (D). It means that electrons are transferred from the D group to the A group in the S_1 state (the top panel of Fig. 1b). Clearly, it is also illustrated that there is a small overlap between the electron and hole distributions in all these three compounds (the bottom panel of Fig. 1b). The overlap between the electron and hole distribution of DEAPF$_6$ is slightly larger than that of TPEPF$_6$ or TPAPF$_6$ according to the S_r and S_m values shown in Table S2.† Combining multiple parameters of electron–hole distribution (Table S2†), all the S_1 states feature ICT characteristics, which is beneficial to the reduction of ΔE_{ST}.[48] The $\Delta E_{S_1-T_1}$ is calculated to be 0.46, 0.46, and 0.56 for TPEPF$_6$, TPAPF$_6$, and DEAPF$_6$, respectively (Fig. 1c and S26†). As shown in Table S3,† all these compounds have small ΔE_{ST}s. Moreover, the results of cyclic voltammetry tests (Fig. S27† and Table 1) are in good accordance with those obtained by Gaussian calculations, all suggesting that TPEPF$_6$, TPAPF$_6$, and DEAPF$_6$ might be good photosensitizers. Encouraged by the theoretical results, a series of experiments were implemented to assess the photophysical and photosensitizing properties, the mitochondria-targeting ability, and the *in vitro* and *in vivo* PDT effect.

Photophysical properties

The photophysical properties of TPEPF$_6$, TPAPF$_6$, and DEPPF$_6$ are summarized in Table 1. Their absorption maximum lies at 419, 476, and 495 nm (Fig. 2a), respectively, and the corresponding molar absorption coefficients are determined to be 3.44×10^4, 3.24×10^4, and 2.81×10^4 L mol^{-1} cm^{-1}. Clearly, the locations of the absorption maxima are compatible with the visible-light excitation source applied in PDT. The emission maximum of TPEPF$_6$, TPAPF$_6$, and DEPPF$_6$ in DMSO is located at 553, 583, and 640 nm, respectively (Fig. 2b). As the solvent polarity increases, their fluorescence intensities gradually decrease with the emission maxima blue- or red-shifted to different degrees (Fig. S28–S30†), reflecting the ICT effect.[53,54] Noteworthily, the solvatochromic effect of TPEPF$_6$ and TPAPF$_6$ is much more significant than that of DEAPF$_6$, which agrees well with the theoretical calculation results.

Their AIE properties were fully demonstrated with the results depicted in Fig. 2c and S31–S42.† They merely showed weak photoluminescence in DMSO (good solvent) in the range of 500–700 nm. As the fraction of toluene (poor solvent) increased, the emission intensities of all these three fluorogens were boosted significantly, attributed to the aggregation-activated restriction of the intramolecular motions (RIM). The emission peaks of TPEPF$_6$, TPAPF$_6$, and DEAPF$_6$ in the DMSO/toluene (1/9, v/v) mixtures are located at 662, 783, and 768 nm, respectively, suggestive of their NIR-fluorescence properties. Their Stokes shifts are over 200 nm and larger than those of the traditional ACQ fluorophores (usually smaller than 50 nm). The large Stokes shift can effectively reduce self-absorption in fluorescence imaging. The transmission electron microscopy (TEM) and dynamic light scattering (DLS) results (Fig. S43–S46†) verified that these NIR-fluorescent compounds all possess AIE properties. Furthermore, as illustrated in Fig. 2b, the emission peaks of TPEPF$_6$, TPAPF$_6$, and DEAPF$_6$ in the solid state are
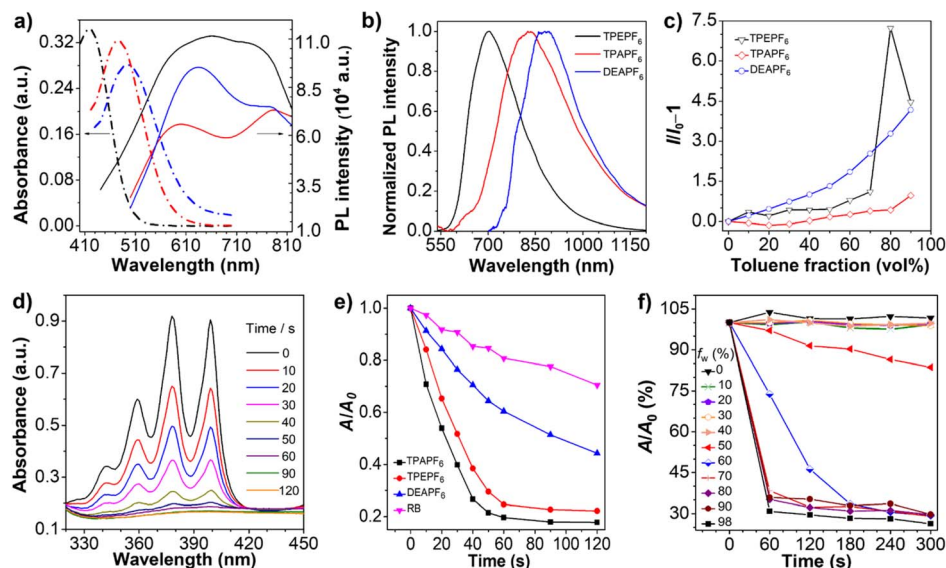
Fig. 2 (a) UV-vis spectra (the dotted lines) and FL spectra (the solid lines) of TPEPF$_6$ (black), TPAPF$_6$ (red), and DEAPF$_6$ (blue) in the dimethyl sulfoxide (DMSO)/toluene (v/v = 1/9) mixtures, respectively, $c = 10^{-5}$ M. (b) Normalized FL spectra of TPEPF$_6$, TPAPF$_6$, and DEAPF$_6$ in the solid state. (c) The plots of the emission enhancements ($I/I_0 - 1$) of TPEPF$_6$, TPAPF$_6$, and DEAPF$_6$ in the DMSO/toluene mixtures *versus* the fractions of toluene, $c = 10^{-5}$ M. (d) UV-vis spectra and (e) decomposition of ABDA in the presence of TPAPF$_6$ after being irradiated with a white light for different times in a mixture of DMSO/water (v/v = 1/100). A_0 = absorption of ABDA @ 378 nm without light irradiation. A = real-time absorbance of ABDA @ 378 nm at different irradiation times. For (d) and (e), to avoid the inner-filter effect, the absorption maxima of the PSs were adjusted to about 0.2 OD. [ABDA] = 5 × [PS]. Light power density = 25 mW cm^{-2} (f) Decomposition rates of ABDA in the presence of TPAPF$_6$ in a mixture of DMSO/water with different water fractions (f_ws) under white-light irradiation ([AIEgen] = 10^{-5} M, [ABDA] = 5 × 10^{-5} M).

located at 694, 833, and 866 nm, respectively. And the fluorescence spectra of TPAPF$_6$ and DEAPF$_6$ even extend over 1200 nm, indicating their potential in the second near-infrared (NIR-II) fluorescence imaging. In addition, the average zeta potential of TPEPF$_6$, TPAPF$_6$, and DEAPF$_6$ in DMSO/water (v/v, 1/99) was measured to be 14.9, 27.9, and 38.1 mV, respectively (Fig. S47†). It thus can be speculated that they might be able to target the mitochondria of living cells.

As shown in Fig. S48,† only small changes were observed in the UV-vis spectra of these three AIEgens (10 μM) under white-light irradiation. The absorbance values remain above 70% even after 15 minutes of continuous white-light irradiation (25 mW cm^{-2}), indicative of their satisfactory photostability.

The crystal data and acquisition parameters of TPAPF$_6$ are summarized in Table S4.† As shown in Fig. S49,† TPAPF$_6$ takes on a highly twisted 3D conformation. Abundant intra- and intermolecular short contacts such as C–H⋯π, C–H⋯F, C–H⋯N interactions, *etc.* significantly stiffen the molecular conformation and restrict the intramolecular motions. Moreover, the distances between the central benzene plane and the pyridinium ring plane of two adjacent molecules are all longer than 3.65 Å, which can prevent the intermolecular π–π stacking, endowing TPAPF$_6$ with outstanding AIE properties.

It is believed that the AIE effect and D–π–A structure tend to promote the generation of ROS.[55,56] As depicted in Fig. 2d, e, and S50,† under white-light irradiation, the absorbance of the ROS indicator, *i.e.*, 9,10-anthracenediyl-bis(methylene)dimalonic acid (ABDA), at 378 nm in the presence of any of these AIEgens significantly decreased with the increasing irradiation

time. The decomposition efficiencies of ABDA coexisting with these AIEgens were significantly higher than that with the commercial PS, *i.e.* Rose Bengal (RB). As calculated, 10.0 nmol of TPEPF$_6$ can degrade 37.7 nmol of ABDA per minute, and the same amount of TPAPF$_6$ and DEAPF$_6$ can degrade 40.2 nmol and 19.8 nmol of ABDA per minute, respectively. The decomposition rate constant of ABDA (κ_{ABDA}) was determined from the curve of ln(A_0/A) *versus* irradiation time (Fig. S51†). The larger the slope, the stronger the ability to generate $^1O_2$. The relative slopes of RB, TPEPF$_6$, TPAPF$_6$, and DEAPF$_6$ are 1.000, 6.597, 8.380, and 2.428, respectively. It suggests that the $^1O_2$ yields of these three AIEgens are all higher than that of RB under parallel conditions. In addition, using RB as a reference (the $^1O_2$ quantum yield is 0.75 in water), the $^1O_2$ quantum yields of TPEPF$_6$, TPAPF$_6$, and DEAPF$_6$ were estimated to be 5.11, 3.17, and 0.88, respectively (Fig. S51†).

The photosensitizing properties evaluation results show good consistency with the results acquired *via* Gaussian and Multiwfn programs. Obviously, compared with DEAPF$_6$, TPEPF$_6$ and TPAPF$_6$ show higher $^1O_2$ quantum yields, which may be related to their different ICT effects and ISC processes.[57] Among all these three AIEgens, the more the rotors, the stronger the $^1O_2$-generating ability is. It might be because the D–π–A-structured AIEgen with more rotors could take on a more twisted conformation which facilitates the electron–hole separation and the differentiation of the electron-cloud distributions at the HOMO and LUMO, thus promoting the ISC. In this manner, the AIE feature not only improves the fluorescence brightness, but also contributes to the generation of ROS in the aggregated state.

Thus, the ability of TPAPF$_6$ to produce $^1O_2$ was studied in mixtures of DMSO/H$_2$O with different water fractions. The results showed that its ability to produce $^1O_2$ is significantly enhanced when the water content exceeds 60% (Fig. 2f and S52†). It is probably because the restriction of intramolecular motions in the aggregated state helps to promote the ISC process, and stabilizes the $^1O_2$. Moreover, the increased amount of oxygen brought by the addition of water might also contribute to the enhanced generation of $^1O_2$.

Mitochondria-specificity and cytotoxicity

Investigation of the intracellular $^1O_2$ generation ability of these three AIE-PSs in 4T1 and SK-OV-3 cells was performed using a SOSG assay.[58–60] As shown in Fig. S53–S58,† strong green fluorescence emerged with the prolongation of the light-irradiation time, indicating their efficient $^1O_2$ production in cells. In addition, the bright-field images showed that the cells cultured by TPEPF$_6$ and TPAPF$_6$ almost all became round, with the cytoplasm becoming leaked and the cytoskeleton destroyed. The cells began to fall off from the culture plates after 15 minutes of white-light irradiation. The morphology of the cells treated with DEAPF$_6$ also changed significantly after 30 min of light irradiation as the cells turned rounded and shrunken. All the above results together exhibited that these AIE-PSs can produce $^1O_2$ at high yields under light irradiation, which can effectively kill cells.

The mitochondria-targeting abilities of these AIE-PSs were assessed as well. The cells treated with our AIE-PSs were clearly visualized with bright red fluorescence, suggesting they enjoy outstanding cell membrane permeability and cell-imaging capabilities. For both 4T1 and SK-OV-3 cells, the fluorescence from AIE-PSs merges well with the fluorescence signal from MitoTracker® Deep Red FM (Fig. S59†). Their Pearson's correlation coefficients are 0.79, 0.84, and 0.75 in 4T1 cells, and 0.79, 0.81, and 0.85 in SK-OV-3 cells, respectively. It showed that these AIE-PSs all hold the ability to target and image the mitochondria of live cells, which may play an important role in tumour treatment.

Motivated by the excellent $^1O_2$ generation efficiency, we further investigated the biocompatibility and photodynamic killing activity of these AIE-PSs through a standard Cell-Counting-Kit-8 (CCK-8) assay. As depicted in Fig. 3, these AIE-PSs show low dark cytotoxicity to both cancer cells and normal cells at a concentration of 10 μM, with all the cell viabilities remaining above 80%. Take TPAPF$_6$ for example. Cell viability does not change significantly in the dark even when the concentration of TPAPF$_6$ is increased to 20 μM, suggestive of good biocompatibility. In sharp contrast, when the cells were exposed to white light for 30 min, the cell survival rates decrease sharply with the increasing concentrations of AIE-PSs. For example, TPEPF$_6$, TPAPF$_6$, or DEAPF$_6$ at a concentration of 10 μM could cause severe viability loss after white-light irradiation, with the cell survival rate of 4T1 cells decreasing to only 12%, 8%, and 24%, respectively. The corresponding half inhibitory concentration (IC$_{50}$) of TPAPF$_6$ to 4T1 cells was as low as 3.98 μM (Table S5†). The IC$_{50}$ of TPEPF$_6$ to A549 and the one of DEAPF$_6$ to 4T1 was 3.12 μM and 3.79 μM, respectively. All the results suggested that these AIE-PSs hold significant photo-cytotoxicity. Similar cytotoxicity has also been found in all examined cells with different AIE-PSs (Fig. 3, S60, and Table S5†). Pitifully, these AIE-PSs show no obvious difference in the phototoxicity to cancer cells and normal cells. As such, intratumoral injection is utilized for the *in vivo* experiments.

Tumour visualization and the antitumor effect

From the viewpoint of excitation/emission wavelength, singlet-oxygen yield, and mitochondria-targeting ability, TPAPF$_6$ holds the best overall performance among all these three AIE-PSs. In other words, although the singlet-oxygen generating ability of TPEPF$_6$ is higher than that of TPAPF$_6$, the absorption and emission maxima of TPAPF$_6$ lie at much longer wavelengths as compared to those of TPEPF$_6$. Moreover, the mitochondria-targeting capability of TPAPF$_6$ is also superior to that of TPEPF$_6$. In view of this, TPAPF$_6$ was selected as a model for the following tumour visualization and antitumor experiments. *In vivo* treatment experiments were carried out based on the 4T1 breast tumour model. As depicted in Fig. 4a, within 1 h after intratumoral injection of TPAPF$_6$, the red fluorescence signal collected with λ_{em} = 700 nm at the tumour sites clearly
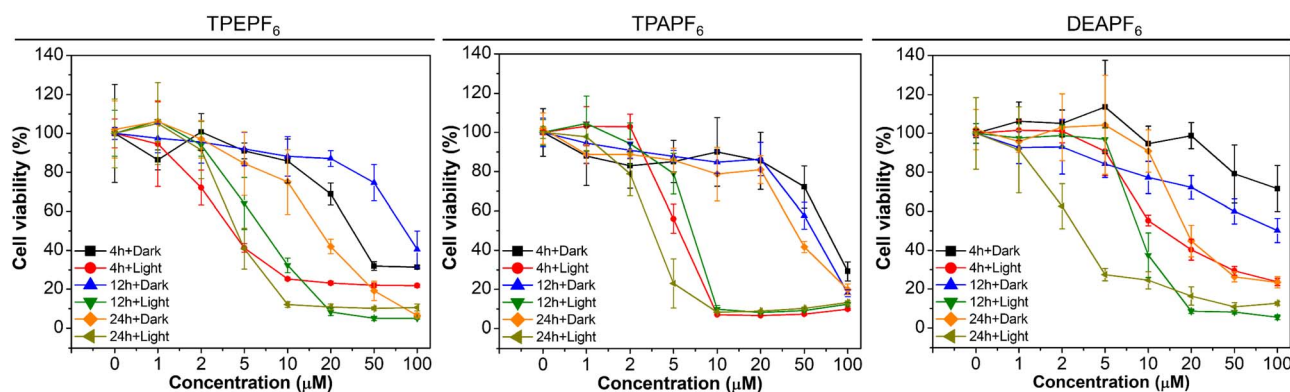

Fig. 3 Relative viabilities of cancer cells (4T1 cells) treated with TPEPF$_6$, TPAPF$_6$, and DEAPF$_6$, respectively, at various concentrations under darkness or white-light irradiation (100 mW cm^{-2}, 30 min) and further being incubated for 4 h, 12 h, or 24 h. Data represent mean value ± standard deviation, n = 6.

Fig. 4 (a) *In vivo* fluorescence visualization of tumour sites (black circles) of the 4T1-bearing BALB/c mice over time after intratumoral administration of TPAPF$_6$. (b) *Ex vivo* fluorescence imaging of tumour tissues and various organs dissected from tumour-bearing mice at 24 h after intratumor injection of TPAPF$_6$ (with or without light irradiation) and PBS. λ_{ex} = 465 nm, λ_{em} = 700 nm. (c) and (d) *In vivo* tumour inhibition effect. (c) Photographs of tumours dissected from tumour-bearing mice after 12 days treatment. (d) Tumour growth curves of mice after different treatments (n = 5). All data are presented as the mean ± SD. The data show significant statistical differences between TPAPF$_6$ + light-treated groups and the other three groups (***P < 0.001, very significant).

demonstrated the accumulation of TPAPF$_6$. Notably, fluorescence emitted from the tumour site was still intense at 24 h post-injection. It is suggestive of the high retention of the TPAPF$_6$ nanoaggregates in cells. Similar results were obtained with the fluorescence signals recorded at λ_{em} = 760 nm (Fig. S61†), further demonstrating the tumour visualizing ability of TPAPF$_6$ with NIR fluorescence. The mice were sacrificed and the fluorescence signals of major organs and tumours were captured to further study the biodistribution of TPAPF$_6$ *in vivo* (Fig. 4b). Among all the evaluated tissues including tumour, heart, liver, spleen, lung, and kidney, no fluorescence signal was observed except from the tumour.

4T1 tumour-bearing mice were applied to evaluate the *in vivo* therapeutic effect of TPAPF$_6$. As illustrated in Fig. S62, 4c and d, the growth of the tumours on the mice injected with PBS and subjected to light irradiation (*i.e.*, PBS + light group) cannot be hindered. Similar results were also shown by the group injected with TPAPF$_6$ but exempt from light irradiation (TPAPF$_6$ group)

and the PBS control group. In sharp contrast, the TPAPF$_6$-treated group showed significantly inhibited tumour growth under white-light irradiation. To further verify the antitumor effect of TPAPF$_6$, 5 mice in each group were sacrificed after 12 days treatment. Then, the tumours were collected, and their volumes and weights were measured (Table S6†). The results shown in Fig. 4c, d, and S63† further proved that TPAPF$_6$ has remarkable antitumor ability *via* PDT.

Moreover, the body weights of mice in each group were measured to assess the *in vivo* biocompatibility. It was found that the body weights of mice among different groups changed reasonably within the normal range during the PDT process, reflecting minimal systemic effects (Fig. S64†). The main organs of mice were collected on day 12 after treatment and stained with H&E dyes. Compared with the PBS group, H&E staining images of major organs in each treated group showed no obvious inflammatory lesions or impairment, and no tissue necrosis was found in any of the histological specimens (Fig. S65a†). Besides that, the

blood of live mice was collected on day 11 post-treatment and the blood biochemical indexes were analysed. As shown in Fig. S65b and c,† the expression levels of aspartate aminotransferase (AST) and blood urea nitrogen (BUN) showed no distinct discrepancy among the four groups, indicating low side effects and satisfactory biocompatibility of $TPAPF_6$. These results provide preliminary evidence that $TPAPF_6$ would not cause acute toxicity during the treatment period, suggestive of its potential for clinical application.

Conclusions

In summary, a series of D–π–A-structured AIE-active PSs, namely $TPEPF_6$, $TPAPF_6$, and $DEAPF_6$, with the electron-donor varying from TPE to TPA and to DEA were facilely synthesized *via* simple procedures. Near-infrared emission and high $^1O_2$ production are achieved by increasing the separation degree of electron–hole distribution, enlarging the difference in the distribution of electron clouds at the HOMO and LUMO, and simultaneously reducing the ΔE_{ST}. Through the investigation of the structure–property relationship, we found that large π-conjugation, strong D–π–A effect as well as sufficient rotors are essential to achieving NIR-emissive and AIE-active photosensitizers with high $^1O_2$ generation ability. Compared with $DEAPF_6$, $TPEPF_6$ and $TPAPF_6$ show higher $^1O_2$ quantum yields. However, the emission wavelengths of $TPAPF_6$ and $DEAPF_6$ are relatively longer than that of $TPEPF_6$, with the solid-state emission spectra extending over 1200 nm. In other words, the emission and photosensitizing properties can be finely tuned by modulating the electron-donating ability and the number of rotors of the electron-donor. Furthermore, their specific targeting capability to mitochondria has also been proven in living cells. These AIE-PSs all show strong ability to kill cells under white-light irradiation even at a low concentration. More importantly, *in vivo* experiments demonstrate that $TPAPF_6$ can achieve visualization of tumour sites with the NIR fluorescence in a high-contrast fashion, and in the meantime can effectively eliminate tumours in a PDT manner. Therefore, our work not only provides some clues on the molecular engineering of highly efficient singlet-oxygen-generating PSs based on AIEgens, but also contributes a series of high-performance PSs with great potential to be used in clinical photo-theranostics.

Data availability

All the data associated with the research in this manuscript are available on reasonable request and can be acquired from the corresponding authors.

Author contributions

J. Mei conceived and designed this work. S. Zhang, W. Yang and Z. Pan conducted the experiments. X. Lu performed the *in vivo* experiments related to tumour visualization and the therapeutic effect. X. Zhang performed the DFT calculation and electron–hole analysis. J. Mei, D. Mei, S. Zhang, H. Tian and D. H. Qu analysed and interpreted the data. J. Mei, S. Zhang, D. Mei and

H. Tian wrote and revised the article. All authors participated in drafting the manuscript and approved the final version of the manuscript.

Conflicts of interest

There are no conflicts to declare.

Acknowledgements

Notes and references

1 T. C. Pham, V.-N. Nguyen, Y. Choi, S. Lee and J. Yoon, *Chem. Rev.*, 2021, **121**, 13454–13619.
2 X. Li, J. F. Lovell, J. Yoon and X. Chen, *Nat. Rev. Clin. Oncol.*, 2020, **17**, 657–674.
3 B. M. Luby, C. D. Walsh and G. Zheng, *Angew. Chem., Int. Ed.*, 2019, **58**, 2558–2569.
4 J. H. Correia, J. A. Rodrigues, S. Pimenta, T. Dong and Z. Yang, *Pharmaceutics*, 2021, **13**, 1332.
5 F. Hu, S. Xu and B. Liu, *Adv. Mater.*, 2018, **30**, 1801350.
6 M. Lan, S. Zhao, W. Liu, C.-S. Lee, W. Zhang and P. Wang, *Adv. Healthcare Mater.*, 2019, **8**, 1900132.
7 R. Vankayala and K. C. Hwang, *Adv. Mater.*, 2018, **30**, 1706320.
8 H. Yu, B. Chen, H. Huang, Z. He, J. Sun, G. Wang, X. Gu and B. Z. Tang, *Biosensors*, 2022, **12**, 348.
9 W. Wu, D. Mao, F. Hu, S. Xu, C. Chen, C.-J. Zhang, X. Cheng, Y. Yuan, D. Ding, D. Konng and B. Liu, *Adv. Mater.*, 2017, **29**, 1700548.
10 M. Wu, X. Liu, H. Chen, Y. Duan, Y. Liu, J. Liu, Y. Pan and B. Liu, *Angew. Chem., Int. Ed.*, 2021, **60**, 9093–9098.
11 J. Dai, Y. Li, Z. Long, R. Jiang, Z. Zhuang, Z. Wang, Z. Zhao, X. Lou, F. Xia and B. Z. Tang, *ACS Nano*, 2020, **14**, 854–866.
12 R. Wang, X. Li and J. Yoon, *ACS Appl. Mater. Interfaces*, 2021, **13**, 19543–19571.

13 P.-C. Lo, M. S. Rodriguez-Morgade, R. K. Pandey, D. K. P. Ng, T. Torres and F. Dumoulin, *Chem. Soc. Rev.*, 2020, **49**, 1041–1056.

14 L. Zhang, Y. Li, W. Che, D. Zhu, G. Li, Z. Xie, N. Song, S. Liu, B. Z. Tang, X. Liu, Z. Su and M. R. Bryce, *Adv. Sci.*, 2019, **6**, 1802050.

15 Y. Jiang, W. Zhu, Z. Xu, Z. Zhang, S. Tang, M. Fan, Z. Li, J. Zhang, C. Yang, W. C. Law, K. T. Yong, D. Wang, G. Xu and B. Z. Tang, *Chem. Eng. J.*, 2022, **448**, 137604.

16 M. Chiba, Y. Ichikawa, M. Kamiya, T. Komatsu, T. Ueno, K. Hanaoka, T. Nagano, N. Lange and Y. Urano, *Angew. Chem., Int. Ed.*, 2017, **56**, 10418–10422.

17 A. Turksoy, D. Yildiz and E. U. Akkaya, *Coord. Chem. Rev.*, 2019, **379**, 47–64.

18 J. Mei, Y. Hong, J. W. Lam, A. Qin, Y. Tang and B. Z. Tang, *Adv. Mater.*, 2014, **26**, 5429–5479.

19 J. Mei, N. L. Leung, R. T. Kwok, J. W. Lam and B. Z. Tang, *Chem. Rev.*, 2015, **115**, 11718–11940.

20 X. Cai and B. Liu, *Angew. Chem., Int. Ed.*, 2020, **59**, 9868–9886.

21 J. Qian and B. Z. Tang, *Chem*, 2017, **3**, 56–91.

22 H. Gao, X. Zhang, C. Chen, K. Li and D. Ding, *Adv. Biosyst.*, 2018, **2**, 1800074.

23 H. Ma, C. Zhao, H. Meng, R. Li, L. Mao, D. Hu, M. Tian, J. Yuan and Y. Wei, *ACS Appl. Mater. Interfaces*, 2021, **13**, 7987–7996.

24 W. Xu, M. M. S. Lee, J.-J. Nie, Z. Zhang, R. T. K. Kwok, J. W. Y. Lam, F.-J. Xu, D. Wang and B. Z. Tang, *Angew. Chem., Int. Ed.*, 2020, **59**, 9610–9616.

25 G. Jiang, C. Li, X. Liu, Q. Chen, X. Li, X. Gu, P. Zhang, Q. Lai and J. Wang, *Adv. Opt. Mater.*, 2020, **8**, 2001119.

26 H. Chen, S. Li, M. Wu, Kenry, Z. Huang, C. S. Lee and B. Liu, *Angew. Chem., Int. Ed.*, 2020, **59**, 632–636.

27 F. Hu, D. Mao, Kenry, X. Cai, W. Wu, D. Kong and B. Liu, *Angew. Chem., Int. Ed.*, 2018, **57**, 10182–10186.

28 H. Shi, X. Pan, Y. Wang, H. Wang, W. Liu, L. Wang and Z. Chen, *ACS Appl. Mater. Interfaces*, 2022, **14**, 17055–17064.

29 H. Wen, Z. Zhang, M. Kang, H. Li, W. Xu, H. Guo, Y. Li, Y. Tan, Z. Wen, Q. Wu, J. Huang, L. Xi, K. Li, L. Wang, D. Wang and B. Z. Tang, *Biomaterials*, 2021, **274**, 120892.

30 W. Wu, D. Mao, S. Xu, M. Panahandeh-Fard, Y. Duan, F. Hu, D. Kong and B. Liu, *Adv. Funct. Mater.*, 2019, **29**, 1901791.

31 Y. Ma, Z. Zhuang, L. Xing, J. Li, Z. Yang, S. Ji, R. Hu, Z. Zhao, Y. Huo and B. Z. Tang, *Adv. Funct. Mater.*, 2021, **31**, 2106988.

32 Z. Liu, H. Zou, Z. Zhao, P. Zhang, G. G. Shan, R. T. K. Kwok, J. W. Y. Lam, L. Zheng and B. Z. Tang, *ACS Nano*, 2019, **13**, 11283–11293.

33 G. Yuan, C. Lv, J. Liang, X. Zhong, Y. Li, J. He, A. Zhao, L. Li, Y. Shao, X. Zhang, S. Wang, Y. Cheng and H. He, *Adv. Funct. Mater.*, 2021, **31**, 2104026.

34 Y. Wang, S. Xu, L. Shi, C. Teh, G. Qi and B. Liu, *Angew. Chem., Int. Ed.*, 2021, **60**, 14945–14953.

35 W. Liu, Z. Li, Y. Qiu, J. Li, J. Yang and J. Li, *ACS Appl. Bio Mater.*, 2021, **4**, 5566–5574.

36 L. Zhang, J. L. Wang, X. X. Ba, S. Y. Hua, P. Jiang, F. L. Jiang and Y. Liu, *ACS Appl. Mater. Interfaces*, 2021, **13**, 7945–7954.

37 S. Liu, G. Feng, B. Z. Tang and B. Liu, *Chem. Sci.*, 2021, **12**, 6488–6506.

38 S. Samanta, Y. He, A. Sharma, J. Kim, W. H. Pan, Z. G. Yang, J. Li, W. Yan, L. W. Liu, J. L. Qu and J. S. Kim, *Chem*, 2019, **5**, 1697–1726.

39 C. Zhou, C. Peng, C. Shi, M. Jiang, J. H. C. Chau, Z. Liu, H. Bai, R. T. K. Kwok, J. W. Y. Lam, Y. Shi and B. Z. Tang, *ACS Nano*, 2021, **15**, 12129–12139.

40 C. Wang, X. Zhao, H. Jiang, J. Wang, W. Zhong, K. Xue and C. Zhu, *Nanoscale*, 2021, **13**, 1195–1205.

41 W. Zhuang, L. Yang, B. Ma, Q. Kong, G. Li, Y. Wang and B. Z. Tang, *ACS Appl. Mater. Interfaces*, 2019, **11**, 20715–20724.

42 Y. F. Xiao, W. C. Chen, J. X. Chen, G. Lu, S. Tian, X. Cui, Z. Zhang, H. Chen, Y. Wan, S. Li and C. S. Lee, *ACS Appl. Mater. Interfaces*, 2022, **14**, 5112–5121.

43 Z. Liu, Q. Wang, W. Qiu, Y. Lyu, Z. Zhu, X. Zhao and W.-H. Zhu, *Chem. Sci.*, 2022, **13**, 3599–3608.

44 D. Wei, Y. Chen, Y. Huang, P. Li, Y. Zhao, X. Zhang, J. Wan, X. Yin, T. Liu, J. Yin, Z. Liu, Q. Zhang, J. Wang and H. Xiao, *Nano Today*, 2021, **41**, 101288.

45 Z. Meng, H. Xue, T. Wang, B. Chen, X. Dong, L. Yang, J. Dai, X. Lou and F. Xia, *J. Nanobiotechnol.*, 2022, **20**, 344.

46 L. Liu, X. Wang, L. J. Wang, L. Guo, Y. Li, B. Bai, F. Fu, H. Lu and X. Zhao, *ACS Appl. Mater. Interfaces*, 2021, **13**, 19668–19678.

47 L. Lin, Z. Wang, J. Fan and C. Wang, *Org. Electron.*, 2017, **41**, 17–25.

48 R. L. X. Gao, M. Barbatti, J. Jiang and G. Zhang, *J. Phys. Chem. Lett.*, 2019, **10**, 1388–1393.

49 X. Tang, L. S. Cui, H. C. Li, A. J. Gillett, F. Auras, Y. K. Qu, C. Zhong, S. T. E. Jones, Z. Q. Jiang, R. H. Friend and L. S. Liao, *Nat. Mater.*, 2020, **19**, 1332–1338.

50 J. Li, T. Nakagawa, J. MacDonald, Q. Zhang, H. Nomura, H. Miyazaki and C. Adachi, *Adv. Mater.*, 2013, **25**, 3319.

51 M. J. Frisch, G. W. Trucks, H. B. Schlegel, G. E. Scuseria, M. A. Robb, J. R. Cheeseman, G. Scalmani, V. Barone, B. Mennucci, G. A. Petersson, H. Nakatsuji, M. Caricato, X. Li, H. P. Hratchian, A. F. Izmaylov, J. Bloino, G. Zheng, J. L. Sonnenberg, M. Hada, M. Ehara, K. Toyota, R. Fukuda, J. Hasegawa, M. Ishida, T. Nakajima, Y. Honda, O. Kitao, H. Nakai, T. Vreven, J. A. Montgomery, J. E. Peralta Jr., F. Ogliaro, M. Bearpark, J. J. Heyd, E. Brothers, K. N. Kudin, V. N. Staroverov, R. Kobayashi, J. Normand, K. Raghavachari, A. Rendell, J. C. Burant, S. S. Iyengar, J. Tomasi, M. Cossi, N. Rega, J. M. Millam, M. Klene, J. E. Knox, J. B. Cross, V. Bakken, C. Adamo, J. Jaramillo, R. Gomperts, R. E. Stratmann, O. Yazyev, A. J. Austin, R. Cammi, C. Pomelli, J. W. Ochterski, R. L. Martin, K. Morokuma, V. G. Zakrzewski, G. A. Voth, P. Salvador, J. J. Dannenberg, S. Dapprich, A. D. Daniels, Ö. Farkas, J. B. Foresman, J. V. Ortiz, J. Cioslowski and D. J. Fox, *Gaussian 09, Revision A02*, Gaussian, Inc., Wallingford CT, 2009.

52 Z. Liu, T. Lu and Q. Chen, *Carbon*, 2020, **165**, 461–467.

53 P. Tan, W. Zhuang, S. Li, J. Zhang, H. Xu, L. Yang, Y. Liao, M. Chen and Q. Wei, *Chem. Commun.*, 2021, **57**, 1046–1049.

54 G. Lin, P. N. Manghnani, D. Mao, C. Teh, Y. Li, Z. Zhao, B. Liu and B. Z. Tang, *Adv. Funct. Mater.*, 2017, **27**, 1701418.

55 H. Zhang, W. Jiang, Y. Peng, J. Yang, X. Chu, Z. Long, R. Li, Q. Liang, H. Suo, S. Wang, M. Yang, J. Qi, D. Ding, Y. W. Yang and B. Wang, *Biomaterials*, 2022, **286**, 121577.

56 W. Wu, L. Shi, Y. Duan, S. Xu, X. Gao, X. Zhu and B. Liu, *Chem. Mater.*, 2021, **33**, 5974–5980.

57 W. Wu, D. Mao, S. Xu, Kenry, F. Hu, X. Li, D. Kong and B. Liu, *Chem*, 2018, **4**, 1937–1951.

58 W. Sun, L. Luo, Y. Feng, Y. Cai, Y. Zhuang, R. J. Xie, X. Chen and H. Chen, *Angew. Chem., Int. Ed.*, 2020, **59**, 9914–9921.

59 D. Zhu, J. Zhang, G. Luo, Y. Duo and B. Z. Tang, *Adv. Sci.*, 2021, **8**, 2004769.

60 K. Zhang, Z. Yu, X. Meng, W. Zhao, Z. Shi, Z. Yang, H. Dong and X. Zhang, *Adv. Sci.*, 2019, **6**, 1900530.